npj | computational materials

www.nature.com/npjcompumats

ARTICLE OPEN

Nonvolatile electrical control of spin polarization in the 2D bipolar magnetic semiconductor VSeF

Yuhui Li[1,2], Jun Deng[1,2], Yan-Fang Zhang[2], Xin Jin[2], Wen-Han Dong[1,2], Jia-Tao Sun[3], Jinbo Pan[1,2,4]✉ and Shixuan Du[1,2,4,5]✉

Nonvolatile electrical control of spin polarization in two-dimensional (2D) magnetic semiconductors is greatly appealing toward future low-dissipation spintronic nanodevices. Here, we report a 2D material VSeF, which is an intrinsic bipolar magnetic semiconductor (BMS) featured with opposite spin-polarized valence and conduction band edges. We then propose a general nonvolatile strategy to manipulate both spin-polarized orientations in BMS materials by introducing a ferroelectric gate with proper band alignment. The spin-up/spin-down polarization of VSeF is successfully controlled by the electric dipole of ferroelectric bilayer Al_2Se_3, verifying the feasibility of the design strategy. The interfacial doping effect from ferroelectric gate also plays a role in enhancing the Curie temperature of the VSeF layer. Two types of spin field effect transistors, namely multiferroic memory and spin filter, are further achieved in VSeF/Al_2Se_3 and VSeF/Al_2Se_3/Al_2Se_3 multiferroic heterostructures, respectively. This work will stimulate the application of 2D BMS materials in future spintronic nanodevices.

npj Computational Materials (2023)9:50 ; https://doi.org/10.1038/s41524-023-01005-8

INTRODUCTION

Two-dimensional (2D) magnetic materials, showing great potential in information storage, transmission and processing by utilizing the spin degree of freedom[1–3], have attracted extensive interests since the experimental discovery of atom-thick magnetic materials CrI_3[4], $Cr_2Ge_2Te_6$[5], and Fe_3GeTe_2[6]. Meanwhile, the sheer openness of 2D magnetic materials makes them possess gate tunability and integrated flexibility[6,7], which is appealing for next-generation nanoscale spintronic devices. In order to develop high-performance 2D spintronic nanodevices, the flexible manipulation of carriers' spin polarization is highly desirable. As compared with the traditional external magnetic field control of spin orientation in materials, electric field control is an extremely exciting research area, both in fundamental science and technology application[8–10], such as exploring multiferroic physics and exploiting the magnetoelectric coupling in ultrafast magnetic memories[11–14]. Recently, magnetic anisotropy[15–17], magnetic conductivity[18–20], magnetic configuration[21–23] and magnetic moment[24] have been reported to be tuned by the ferroelectric polarization via interfacial magnetoelectric effects.

Bipolar magnetic semiconductors (BMSs), whose valence band maximum (VBM) and conduction band minimum (CBM) are derived from opposite spin channels, offer an ideal platform to achieve the electrical manipulation of both spin orientation around Fermi energy[25,26]. Till now, only a few intrinsic 2D BMSs have been theoretically predicted[27–32], where the origins of bipolar semiconducting character are complicated and remain to be further explored. On the other hand, the state-of-the-art proposed way to manipulate carriers' spin-polarized orientation in BMS materials requires persistent electrical control which is volatile and achieved by applying a gate voltage[19,26,33]. Thus, designing 2D BMSs, exploring the formation mechanism of the bipolar semiconducting properties, and realizing nonvolatile control of the carriers' spin polarization are crucial for 2D BMSs' application. That will stimulate and accelerate the future development of 2D BMS materials in 2D spintronics.

In this work, we first report an intrinsic 2D BMS VSeF with a strongly correlated charge-transfer-type electronic band structure, where the hole effective mass is far less than the electron effective mass. Inspired by the ferroelectric (FE) materials with spontaneous electric polarization, we propose a general strategy to achieve nonvolatile manipulation of the carriers' spin polarization in BMSs by introducing a FE gate with proper band alignment. Using first-principles calculation, our proposal has been achieved in the BMS VSeF monolayer by putting it on 2D FE Al_2Se_3 layer, considering the lattice mismatch. As stacked on a single-layer FE Al_2Se_3, monolayer VSeF preserves its BMS character when Al_2Se_3 (↓) is downward electric polarized, while it transforms into a half-metal upon reversing the electric polarized orientation of Al_2Se_3 (↑). To induce a larger built-in electric field, we increase the thickness of the FE layer to bilayer Al_2Se_3. It is found that the VSeF is n-doped with spin-up carriers by the upward electric polarization of bilayer Al_2Se_3 (↑), while it's p-doped with spin-down carriers by the downward electric polarization of bilayer Al_2Se_3 (↓). Due to the interfacial doping effect, the Curie temperature of VSeF can be enhanced from 66 K to 71 K, 76 K and 81 K in VSeF/Al_2Se_3 (↑), VSeF/biAl_2Se_3 (↓) (bilayer Al_2Se_3) and VSeF/biAl_2Se_3 (↑), respectively. Based on these multiferroic van der Waals (vdW) heterostructures, we further design two types of spin field effect transistors (FETs), namely few-layer multiferroic memory and spin filter, using VSeF/Al_2Se_3 bilayer heterostructure and VSeF/biAl_2Se_3 trilayer heterostructure, respectively. We find that the choices of FE gates are abundant. Different FE gates would lead to different carriers' doping concentrations. Our results pave the way for the realization and application of 2D BMS in future spintronic nanodevices.

[1]Beijing National Laboratory for Condensed Matter Physics, Institute of Physics, Chinese Academy of Sciences, 100190 Beijing, China. [2]University of Chinese Academy of Sciences, Chinese Academy of Sciences, 100190 Beijing, China. [3]School of Integrated Circuits and Electronics, MIIT Key Laboratory for Low-Dimensional Quantum Structure and Devices, Beijing Institute of Technology, 100081 Beijing, China. [4]Songshan Lake Materials Laboratory, 523808 Dongguan, China. [5]CAS Center for Excellence in Topological Quantum Computation, 100190 Beijing, China. ✉email: jbpan@iphy.ac.cn; sxdu@iphy.ac.cn

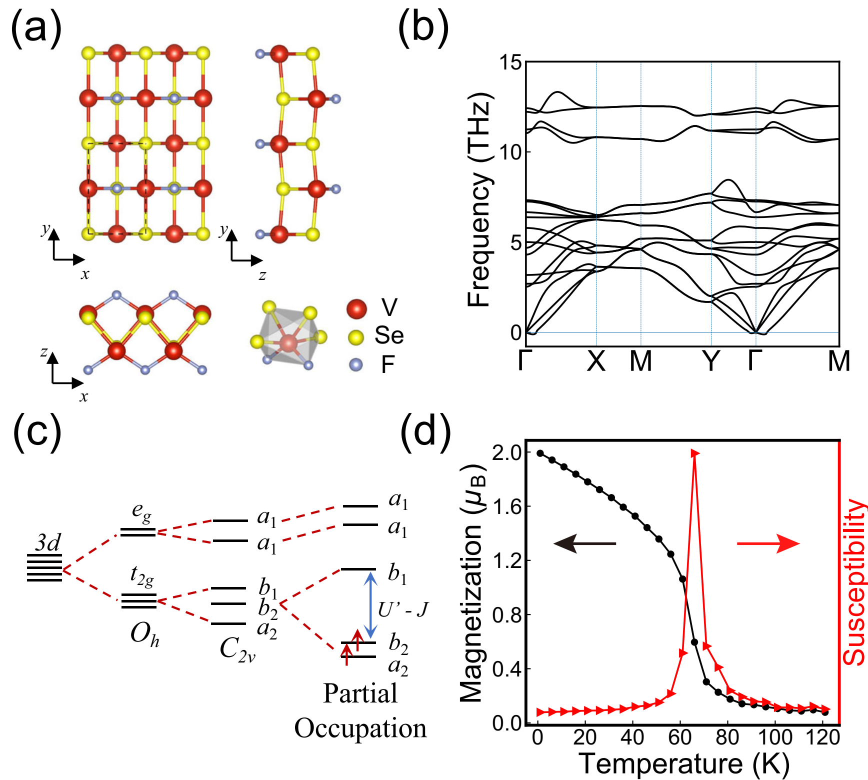

Fig. 1 Structure and magnetic properties of VSeF monolayer. a Top and side views of VSeF monolayer, and a local distorted VSe_4F_2 octahedron. Red, yellow, and gray balls represent V, Se, and F atoms, respectively. **b** Phonon spectrum of VSeF monolayer. **c** The 3*d* orbital splitting from an ideal octahedron with O_h symmetry to a distorted octahedron with C_{2v} symmetry, and further splitting with a larger energy gap between occupied states and unoccupied states in V^{3+} $3d^2$ due to the electronic correlation. **d** Simulated magnetic moment (black data) and magnetic susceptibility (red data) as functions of temperature for 2D VSeF.

RESULTS

Structure and magnetic properties of VSeF monolayer

The crystal structure of the VSeF monolayer, as depicted in Fig. 1a, consists of buckled double VSe layers sandwiched by two F atomic layers. The VSeF monolayer crystallizes in the orthorhombic symmetry group (space group *Pmmn*), which takes the same structure as the experimentally synthesized 2D magnetic semiconductor CrSBr[34]. VSeF monolayer is screened from *MXY* compounds (M = Ti, V, Cr, Mn, Fe, Co, Ni, X = O, S, Se, Te, Y = F, Cl, Br, I), taking CrSBr as prototype structure. The calculated results are summarized in Supplementary Table 1, containing stable nonmagnetic metals, nonmagnetic semiconductors, magnetic metals and magnetic semiconductors. Among them, only VSF and VSeF are dynamically stable 2D bipolar magnetic semiconductors (BMS). Supplementary Fig. 1 presents the electronic band structure and phonon spectrum of VSF, which is similar with that of VSeF. The calculated lattice parameters of VSeF monolayer are listed in Supplementary Table 2. Phonon spectrum calculation was performed. As shown in Fig. 1b, no imaginary frequency is observed in the phonon spectrum, indicating that VSeF monolayer is dynamically stable. The thermal stability of VSeF monolayer is evaluated by performing ab initio molecular dynamical (AIMD) simulations at 300 K and 500 K. The geometric structure of the VSeF monolayer at different temperatures keeps intact (Supplementary Fig. 2), which indicates that VSeF monolayer is thermally stable. The thermodynamical stability of VSeF monolayer is evaluated by performing a global structure optimization for 2D V-Se-F crystal via CALYPSO code[35,36], and investigating its energy above convex hull. We didn't find other structures which have lower formation energies than that of our studied structure after 15-generation optimizations. In addition, the energy above convex hull obtained from the Computational 2D Materials Database (C2DB) is only 0.14 eV/atom, lower than the thermodynamical stability criteria of 0.2 eV/atom in previous literatures[37,38]. These results thus indicate that VSeF monolayer is thermodynamically stable.

The magnetic property of VSeF monolayer is largely dependent on the local environment of V^{3+}. Each V^{3+} is surrounded by four Se^{2-} and two F^- forming a distorted octahedron VSe_4F_2 with C_{2v} symmetry. As illustrated in Fig. 1c, under an ideal octahedral crystal field with O_h symmetry, the fivefold degenerate *d* orbitals split into double degenerate e_g orbitals and threefold degenerate t_{2g} orbitals. In VSeF, the distorted octahedral crystal field further lifts double degenerate e_g orbitals into two a_1 orbitals, and threefold degenerate t_{2g} orbitals into b_1, b_2, and a_2 orbitals. The two V^{3+} d^2 electrons occupy two of three nearly degenerate orbitals (b_2 and a_2 orbitals), which is different from the situation in CrSBr[39]. In the case of Cr^{3+} d^3 orbitals, the three nearly degenerate orbitals (b_1, b_2, and a_2 orbitals) are half-filled, which can be described by the nondegenerate single-band Hubbard model. However, the physical picture of the partial occupation of degenerate orbitals needs to be described by a multiband Hubbard model.

The multi-orbital Hamiltonian is given as

$$H = -t\sum_{<ij>,m\sigma}\left(d^{\dagger}_{im\sigma}d_{jm\sigma} + h.c.\right) + \sum_{i,m\sigma}\varepsilon_m d^{\dagger}_{im\sigma}d_{im\sigma} + U\sum_{i,m} n_{im\uparrow}n_{im\downarrow} + \left(U' - \frac{J}{2}\right)\sum_{i,m>m'} n_{im}n_{im'} - J\sum_{i,m>m'} 2\mathbf{S}_{im}\cdot\mathbf{S}_{im'} \quad (1)$$

where *i* and *j* represent the two neighboring magnetic sites, *m* and *m′* are the orbital indexes. The first term describes the nearest-

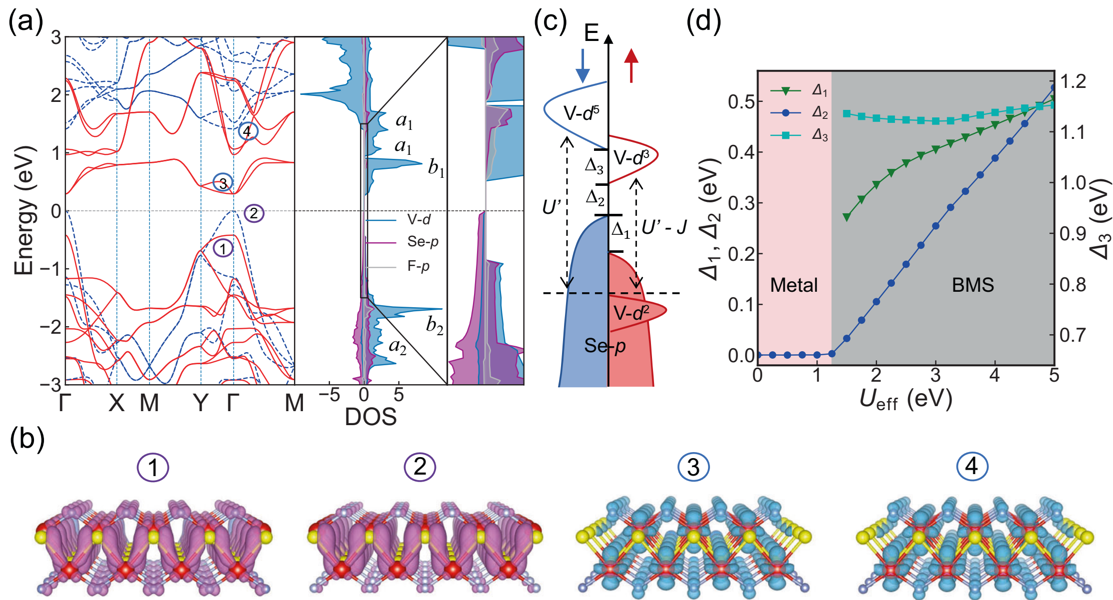

Fig. 2 Electronic structures and the origin of BMS. a Spin-resolved band structure where red lines and blue dashed lines represent spin-up and spin-down channels, respectively, element-resolved PDOS of VSeF monolayer and zoom-in PDOS near the Fermi level where blue, magenta, and gray regions represent the PDOS contributed by V, Se, and F atoms, respectively. Fermi level is set to 0 eV, as labeled by horizontal black dashed line. **b** Partial charge densities of VBMs and CBMs of both spin channels. The marked numbers correspond to band decomposed locations in panel a. The magenta and blue isosurfaces represent the electron densities of VBMs and CBMs, respectively, where the isosurface value is 4×10^{-3} e·bohr^{-3}. **c** Schematic spin-resolved DOS of VSeF monolayer with the BMS behavior where the red and blue colors represent spin-up and spin-down channel, respectively, and the BMS feature can be described by three energy parameters (Δ_1, Δ_2, and Δ_3). Δ_2 is the bipolar bandgap. **d** The variations of three energy parameters (Δ_1, Δ_2, and Δ_3) as the $U_{eff} = U - J$ parameter. When U_{eff} is less than 1.25 eV, VSeF is a metal ($\Delta_2 = 0$; the pink region). Once U_{eff} is larger than 1.25 eV, VSeF is a BMS (the gray region).

neighbor hopping, the second term describes the on-site orbital energies, the third to fifth terms are the intra- (U) and interorbital (U') Coulomb interactions and the Hund's coupling (J), where $U' = U - 2J$[40,41]. Single-band Hubbard model only contains the first three items of Eq. (1), completely neglecting the interorbital Coulomb interactions. However, when the strongly correlated degenerate orbitals are partially filled, the interorbital repulsion between occupied orbitals and unoccupied orbitals ($U' - J$) cannot be neglected, which is crucial to decide the electronic structure (Fig. 1c). Similar cases have been reported in VS_2[42], VI_3[43], VOCl[44], TiOCl[41], etc. In VI_3 (V^{3+} with d^2 electronic configuration), the Hubbard U value shifts up (down) the unoccupied (occupied) orbital levels producing a semiconducting character[43].

The two d^2 electrons of V^{3+} in VSeF produce a local magnetic moment of 2 μ_B, which is in accordance with the results from DFT calculations. To determine the magnetic ground state of VSeF monolayer, we considered five possible magnetic configurations (Supplementary Fig. 3). It is found that the ferromagnetic state is the most stable configuration. And the ferromagnetic ground state of VSeF is robust against the Hubbard U (Supplementary Fig. 5) and spin-orbit coupling (SOC) effect (Supplementary Table 3). The easy axis of magnetization of VSeF monolayer is along the out-of-plane direction, whose energy is lower than that of the in-plane direction (Supplementary Table 4). Based on the classical Heisenberg Hamiltonian,

$$H = -\sum_{i\neq j} J_1 \mathbf{S}_i \cdot \mathbf{S}_j - \sum_{i\neq k} J_2 \mathbf{S}_i \cdot \mathbf{S}_k - \sum_{i\neq m} J_3 \mathbf{S}_i \cdot \mathbf{S}_m + \sum_i A_x \left(S_i^x\right)^2 + \sum_i A_y \left(S_i^y\right)^2 \quad (2)$$

where J_1, J_2, and J_3 are the nearest, next-nearest and third-nearest-neighbor exchange interaction parameters, respectively. A_x and A_y represent to single-ion anisotropy along the x and y direction, respectively. These parameters can be extracted by comparing the relative energies of different magnetic configurations (Supplementary Table 4). We carried out Monte Carlo simulation to estimate the Curie temperature (T_c) by using a 50 × 50 superlattice. The susceptibility is calculated according to $\chi = (\langle E^2\rangle - \langle E\rangle^2)/(k_B T)$. The calculated magnetization and susceptibility indicate that the Curie temperature is around 66 K (Fig. 1d), which is higher than that of the experimentally known T_c of 2D magnetic semiconductor CrI_3 (45 K).

Electronic structures and the origin of BMS

The electronic band structure of VSeF calculated by the GGA + U ($U_{eff} = 3.25$ eV) shows that the VSeF monolayer behaves as a BMS, where the VBM and CBM are derived from different spin channels (Fig. 2a). As the HSE06 functional generally gives more accurate band structures for semiconductors, we also calculated the band structure of VSeF by using an HSE06 functional (Supplementary Fig. 6), which is qualitatively consistent with the result from GGA + U calculation, indicating that the BMS character of VSeF is robust. Since the Se atom is heavy, the spin-orbit coupling (SOC) effect may affect the electronic structure of VSeF, we further calculated the electronic band structure including the SOC effect. The calculated band structure (Supplementary Fig. 7) exhibits bipolar character, which is consistent with that obtained without considering SOC effect. The spin-resolved projected density of states (PDOS) shows that the VBMs of both spin channels are mainly contributed by Se-p orbitals, and the CBMs are mainly contributed by V-d orbitals (Fig. 2a). That is in accordance with the partial charge densities of VBMs and CBMs of both spin channels (Fig. 2b). The charge densities of VBMs of both spin channels (①: spin up channel; ②: spin down channel) are similar, showing the main Se-p_x orbital feature and partial Se-p_x and V-d_{xz} bonding feature. The charge densities of CBMs of both spin channels (③: spin up channel; ④: spin down channel) which are mainly localized in V atoms are also similar.

The BMS feature of VSeF can be described by three energy gaps (Δ_1, Δ_2, and Δ_3), as shown in Fig. 2c. The Δ_2 gap is defined as the spin-flip gap between the VBM and CBM from different spin channels. $\Delta_1 + \Delta_2$ and $\Delta_2 + \Delta_3$ represent the spin-conserved gaps for two spin channels, respectively. Fig 2c depicts the schematic density of states (DOS) of VSeF, where the Se-*p* orbital bands with broad bandwidth are full-occupied, while the V-*d* orbital bands are partially occupied and localized. According to the aforementioned multiband Hubbard model, the orbital repulsion between the occupied states and unoccupied states with the same spin orientation is $U' - J$, while the orbital repulsion between the occupied states and unoccupied states from different orbitals with different spin orientation is U'. Therefore, we investigated the influence of the effective Hubbard U parameter U_{eff} on the band structure of VSeF. As shown in Supplementary Fig. 8, the splitting between occupied V-*d* orbitals and unoccupied V-*d* orbitals gradually increases with U_{eff} value, and a transition from metal to BMS happens when U_{eff} equals 1.25 eV, indicating the strongly correlated characteristic of VSeF. When U_{eff} equals 0, VSeF is a metal where the *d*-orbital splitting originated from the distorted crystal field is small. Increasing the U_{eff} value gradually enhances the interorbital splitting between occupied and unoccupied orbitals, inducing a semiconducting bandgap. The magnitude of the three energy gaps (Δ_1, Δ_2, and Δ_3) as a function of U_{eff} are summarized in Fig. 2d. In the BMS region, Δ_1 and Δ_2 gradually increase with U_{eff} value, while Δ_3 is less affected. That's in accordance with the depicted picture in Fig. 2c.

It is worth noting that VSeF is a charge-transfer semiconductor, where the hole effective mass is smaller than the electron-effective mass[45]. Therefore, the carrier mobility of VSeF is largely dependent on the carrier type. Here, due to the broken time-reversal symmetry in ferromagnetism, the spin-up channels of valence band (VB) and conduction band (CB) together downward shift, while the spin-down channels upward shift, lifting Kramer's degeneracy. Therefore, the VBM and CBM of VSeF are derived from the opposite spin channel. Δ_1 and Δ_3 are the spin exchange splitting gaps of VB and CB, respectively. Due to the partial hybridization between Se-p_x orbitals and V-d_{xz} orbitals in VBMs, the spin splitting gap Δ_1 is moderate. The origin of BMS in VSeF is different from the BMS formation mechanism of other transition metal compounds proposed by Deng et al., where the bipolar bandgap Δ_2 is derived from the spin exchange splitting of the same *d* orbital[28,46].

Monolayer Al_2Se_3 ferroelectric gate

The electronic structure of BMS enables electrical fields to control the carriers' spin-polarization directions. It's common to manipulate the spin polarization of BMS materials by applying a gate voltage (Supplementary Fig. 9). The 100% spin-polarized channel currents can be realized by changing the sign of the applied gate voltage. Supplementary Fig. 10 shows the variation of band structure of VSeF with the carrier concentrations. Upon hole (electron) doping, the spin-down (spin-up) carriers dominate the Fermi level. Besides, VSeF monolayer always keeps the ferromagnetic magnetic ground state under different carrier doping concentrations (Supplementary Fig. 11). However, the realization of electrical control of spin polarization by applying a gate voltage in BMS materials remains to be explored in the experiment. And this way to control carriers' spin polarization is volatile, requiring a persistent external electrical field.

To solve these problems, we proposed that it's possible to manipulate the spin polarization of BMS materials by applying a ferroelectric gate, as shown in Fig. 3a. Ferroelectric materials exhibit spontaneous polarization which can be maintained even if removing the external electric field. And the ferroelectric polarization can be switched by applying a short-term pulse voltage. Due to the built-in electric field induced by the ferroelectric polarization, the energy band alignment between ferroelectric dielectric layer and BMS channel layer can be altered by switching the direction of ferroelectric polarization. Consequently, the charge transfer between ferroelectric layer and BMS layer is also tunable (Fig. 3a). When the VBM of FE locates within the CBMs of spin-up and spin-down channel of BMS, n-type doping occurs in BMS, and electron carriers possess spin-up orientation. When the CBM of FE locates within the VBMs of spin-up and spin-down channel of BMS, p-type doping occurs in BMS, and hole carriers possess spin-down orientation. Therefore, nonvolatile electrical control of spin polarization is expected to be realized by constructing multiferroic BMS/FE heterostructures. This way can overcome the volatility in traditional electrical control approaches, which is more energy-efficiency.

To verify the proposal, we first constructed a multiferroic vdW heterostructure for the predicted 2D BMS VSeF by combining a 2D ferroelectric Al_2Se_3, as shown in Fig. 3b. Single-layer Al_2Se_3 possesses the same structure as α-In_2Se_3 monolayer with hexagonal symmetry group[47], which is screened from the family of 2D ferroelectric III_2-VI_3 materials by considering the band alignments and lattice mismatch between VSeF monolayer and 2D III_2-VI_3 ferroelectrics (Supplementary Fig. 12). The ferroelectric polarization state depends on the movement of the middle Se layer. When the middle Se atom is close to the bottom (upper) Al atom, it's upward (downward) polarization P↑(P↓). Considering the lattice mismatch, the relaxed $\sqrt{3}\times 3$ -Al_2Se_3 supercell with orthorhombic lattice is strained by 2.3% (*x* direction) and -6.8% (*y* direction) to match the 2 × 2-VSeF. To evaluate the stability of Al_2Se_3 ferroelectric state under strained, we calculated the entire ferroelectric polarization reversal path of strained Al_2Se_3 to compare the energy difference between the centrosymmetric phase and ferroelectric phase. As shown in Supplementary Fig. 13, the ferroelectric state of strained Al_2Se_3 is still more stable than the paraelectric phase. We considered 24 possible stacking mode between VSeF and Al_2Se_3 by shifting their relative positions in the in-plane direction. As shown in Supplementary Fig. 14, by comparing the total energies of these 24 configurations, the most stable structures are obtained, which are the same for both P↑ and P↓.

In our calculations, we fixed the lattice constant of VSeF and only relaxed the atomic positions in heterostructures for eliminating the strain influences on the BMS properties of VSeF. Due to the built-in electric field, there is a potential drop of 1.73 eV across the two sides of Al_2Se_3 (Supplementary Fig. 15), which produces different band alignments when VSeF contacts with P↑ and P↓ Al_2Se_3. As illustrated in Fig. 3c, the different band alignments lead to different interfacial charge transfer. When combined with P↑ Al_2Se_3, the potential energy of VSeF is lower than that of Al_2Se_3 (Supplementary Fig. 16a), which makes that the spin-up CBM of VSeF is lower than the VBM of Al_2Se_3, suggesting that electrons can transfer from Al_2Se_3 to spin-up channel of VSeF. In contrast, for VSeF/Al_2Se_3 (↓), the potential energy of Al_2Se_3 is lower (Supplementary Fig. 16b), but the CBM of Al_2Se_3 is still slightly higher than the spin-down VBM of VSeF. Therefore, the electrons transfer from VSeF to Al_2Se_3 is blocked.

The calculated layer-resolved PDOS are consistent with the analysis of band alignments. As indicated in Fig. 3d, in VSeF/Al_2Se_3 heterostructure, the potential energy decreases along the direction of black dashed arrow, leading to the band relative shift between VSeF and Al_2Se_3. We found that the half-metallicity with spin-up polarization appears in the VSeF part of VSeF/Al_2Se_3 (↑) heterostructure, showing n-type doping feature. In contrast, VSeF remains as a semiconductor, when combined with P↓ Al_2Se_3. Therefore, the ferromagnetic half-metal/semiconductor switching in VSeF can be controlled by the polarized states of the Al_2Se_3 monolayer.

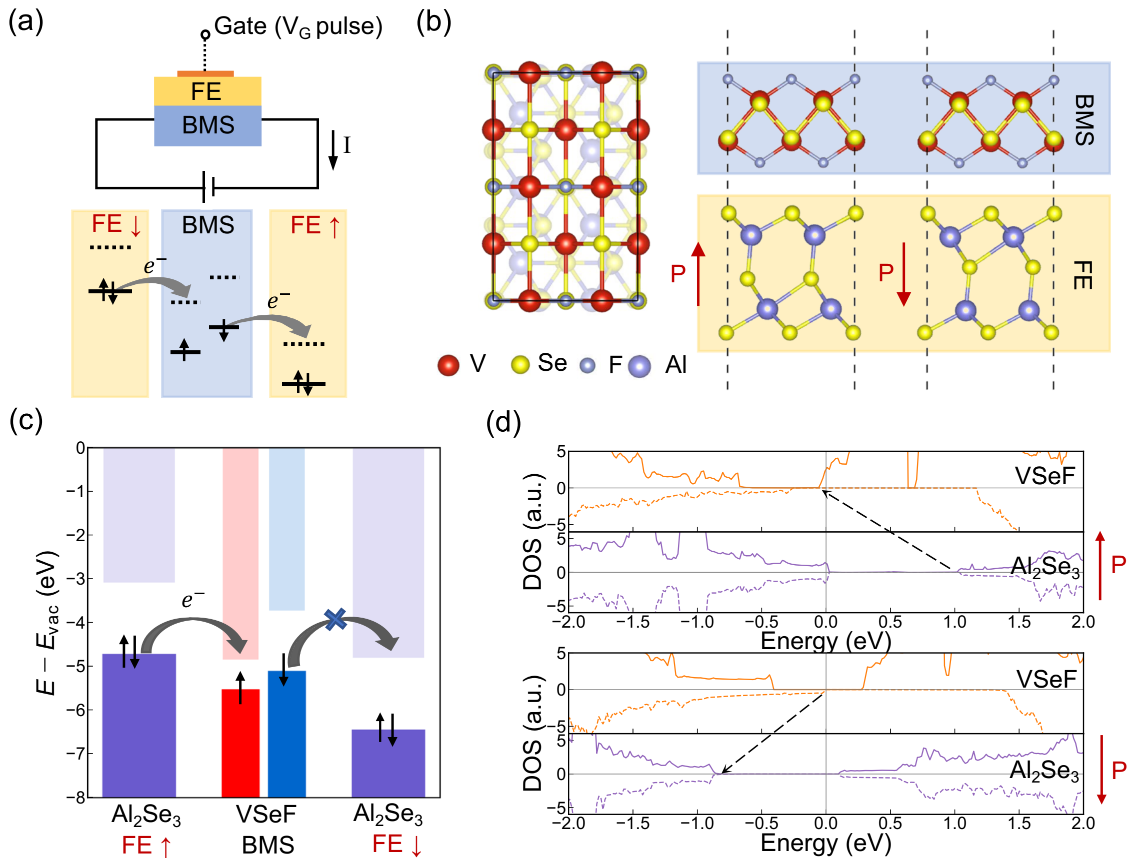

Fig. 3 Manipulation of BMS by the ferroelectric gate and VSeF/Al_2Se_3 bilayer heterostructures. a Schematic diagram of spin FET based on BMS, the spin orientations in the conducting channel (BMS region, marked in blue) can be controlled by switching the electric polarization of ferroelectric dielectric (FE region, marked in yellow). The bottom panel depicts the desired band alignments between BMS and FE under different ferroelectric polarized states, and associated charge transfers. Here, the solid and dashed lines represent VBM and CBM, respectively. Black arrows denote the electron spin, where electrons fill to the VBMs. The spin-up and spin-down bands of BMS are split, due to the intrinsic magnetism of BMS. **b** Top and side views of VSeF/Al_2Se_3 bilayer heterostructures. The red arrow represents the polarization direction of Al_2Se_3. **c** Band alignments of VSeF/Al_2Se_3 (↑) and VSeF/Al_2Se_3 (↓) with respect to the vacuum level of VSeF. The red and blue bars show the band edges of spin-up and spin-down channels of BMS, respectively, the purple bars show the band edges of FE. **d** Layer-resolved PDOS of VSeF/Al_2Se_3 (↑) and VSeF/Al_2Se_3 (↓), where the orange and purple lines represent the PDOS contributed by VSeF and Al_2Se_3, respectively. The potential energy decreases along the direction of black dashed line.

Bilayer Al_2Se_3 ferroelectric gate

To realize nonvolatile electrical control of spin polarization in VSeF, we further tried to stack VSeF on the bilayer Al_2Se_3 forming a trilayer vdW heterostructure (Fig. 4a), where the bilayer Al_2Se_3 possesses enhanced ferroelectric polarization[47,48]. Similar to VSeF/Al_2Se_3 bilayer heterostructure, we first calculated the band alignments for VSeF/biAl_2Se_3 (↑) and VSeF/biAl_2Se_3 (↓). As shown in Fig. 4b, the band alignments between VSeF and neighbor Al_2Se_3 (FE1) are less affected by the added bottom Al_2Se_3 (FE2), which are similar to that of VSeF/Al_2Se_3 bilayer heterostructure. Particularly, due to the built-in electric field, there also exists charge transfer between bilayer Al_2Se_3. To visualize the charge redistribution in VSeF/biAl_2Se_3 heterostructure, the charge density difference, plane-averaged charge density difference ($\Delta\rho$) and the z-direction integral of plane-averaged charge density difference (n) are shown in Fig. 4c, d for VSeF/biAl_2Se_3 (↑) and VSeF/biAl_2Se_3 (↓), respectively. The negative $\Delta\rho$ represents the charge depletion and the positive $\Delta\rho$ represents the charge accumulation.

Clearly, the charge transfer not only occurs between VSeF and FE1, but also between FE1 and FE2. The z-direction integral of plane-averaged charge density difference indicates that the total charge depletion and accumulation of each layer mainly occur within VSeF and FE2, and the variation of total charge of FE1 is small. Therefore, it can be equivalently viewed that the charge transfer mainly happens between VSeF and FE2, where the FE1 acts as a bridge. As reflected in the layer-resolved PDOS (Fig. 4e, f), because the effective charge transfer occurs within VSeF and FE2, both VSeF and FE2 exhibit metallicity, while FE1 always remains as a semiconductor. Interestingly, n-doped VSeF with spin-up carriers appears in VSeF/biAl_2Se_3 (↑) heterostructure, and p-doped VSeF with spin-down carriers appears when reversing the ferroelectric polarization of bilayer Al_2Se_3. Therefore, nonvolatile electric control of spin polarization is achieved in VSeF/biAl_2Se_3 trilayer heterostructure. Different spin-orientation channel current in VSeF can be switched by the polarized states of bilayer Al_2Se_3.

Doping effect on VSeF from FE substrates

It's worth noting that the VSeF layer always maintains the ferromagnetic ground state and out-of-plane easy magnetization axis in all heterostructures, as shown in Supplementary Table 4, the energies of out-of-plane ferromagnetic configuration are lowest for whichever heterostructure. Due to the interfacial engineering on magnetism[49,50], we further explored the influence of FE substrates on the Curie temperature of VSeF. As shown in Figs. 5a, b, the T_c value of VSeF is enhanced to 71 K, 76 K and 81 K in VSeF/Al_2Se_3 (↑), VSeF/biAl_2Se_3 (↓) and VSeF/biAl_2Se_3 (↑)

Fig. 4 VSeF/biAl$_2$Se$_3$ trilayer heterostructures. **a** Side views of VSeF/biAl$_2$Se$_3$ trilayer heterostructures. The red arrow represents the polarization direction of Al$_2$Se$_3$. **b** Band alignments of VSeF/biAl$_2$Se$_3$ (↑) and VSeF/biAl$_2$Se$_3$ (↓) with respect to the vacuum level of VSeF. The red and blue bars depict the band edges of spin-up and spin-down channel of VSeF, respectively. The purple bars depict the band edges of two layers of FE Al$_2$Se$_3$. **c**, **d** Charge density difference, planar-averaged density difference (black line) and the integral (red lines) of planar-averaged density difference along *z*-direction for VSeF/biAl$_2$Se$_3$ (↑) and VSeF/biAl$_2$Se$_3$ (↓), respectively, where the blue dashed lines indicate the atomic boundary of each layer, and the cyan and magenta isosurfaces represent electronic accumulation and depletion with isovalue of 2.03×10^{-3} e Å^{-3}, respectively. **e**, **f** Layer-resolved PDOS of VSeF/biAl$_2$Se$_3$ (↑) and VSeF/biAl$_2$Se$_3$ (↓). The potential energy decreases along the direction of black dashed line. FE1 and FE2 denote the upper Al$_2$Se$_3$ layer and the bottom Al$_2$Se$_3$ layer, respectively. The orange, purple, and pink lines represent the PDOS contributed by VSeF, FE1, and FE2, respectively.

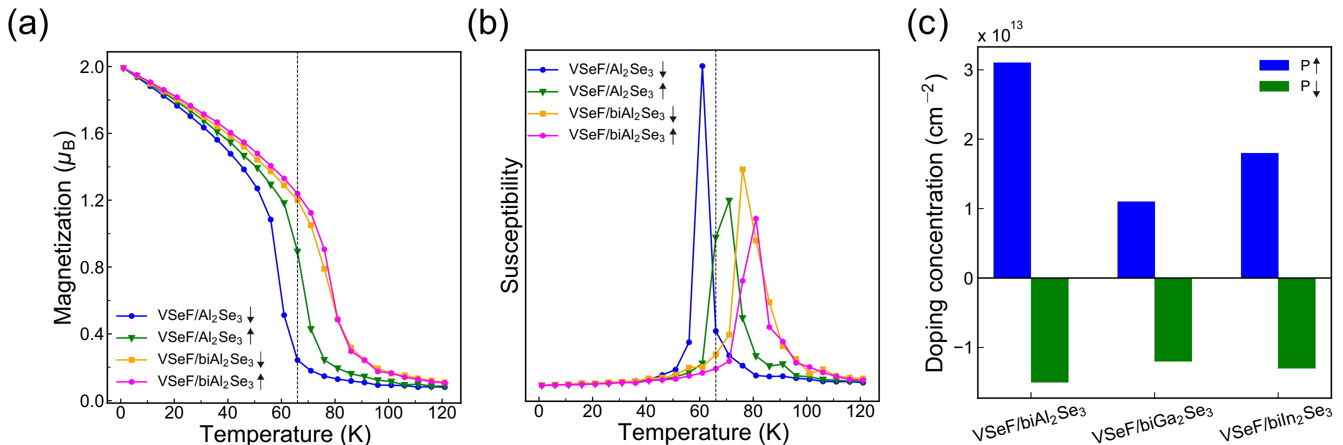

Fig. 5 Doping effect on VSeF layer from FE gates. **a**, **b** The variations of magnetic moment and susceptibility as functions of temperature in VSeF/Al$_2$Se$_3$ (↓) (blue line), VSeF/Al$_2$Se$_3$ (↑) (green line), VSeF/biAl$_2$Se$_3$ (↓) (orange line) and VSeF/biAl$_2$Se$_3$ (↑) (magenta line) heterostructures. The black dashed line indicates the T_c value of pristine VSeF monolayer. **c** The doping concentration of VSeF layer under different FE substrates (bilayer Al$_2$Se$_3$, bilayer Ga$_2$Se$_3$ and bilayer In$_2$Se$_3$) and FE polarized states (upward polarization or downward polarization). The blue and green bars depict the doping concentrations from upward and downward electric polarized FE gates, respectively. The positive and negative doping concentration indicate electron and hole doping, respectively.

heterostructures, respectively. While for the $VSeF/Al_2Se_3$ (↓) heterostructure, the T_c value is slightly decreased to 61 K. Since the lattice constants of VSeF layer are fixed in all heterostructures and the structure variations of VSeF layer are minor (Supplementary Table 5 and Supplementary Fig. 4), the change of T_c value can be primarily attributed to the interfacial charge transfer between VSeF and FE substrates. VSeF layer is n-type doped in $VSeF/Al_2Se_3$ (↑) and $VSeF/biAl_2Se_3$ (↑) heterostructures, and p-type doped in $VSeF/biAl_2Se_3$ (↓) heterostructure, exhibiting ferromagnetic half-metallic property. However, VSeF layer keeps its ferromagnetic semiconducting property in $VSeF/Al_2Se_3$ (↓) heterostructure. Generally, due to the existence of itinerant carriers, ferromagnetic metals possess higher Curie temperatures than that of ferromagnetic semiconductors[4–6].

By calculated the charge density difference (Fig. 4c, d and Supplementary Fig. 17a, b), we also quantitatively analyzed the doping concentrations of Al_2Se_3 gates under different layer numbers and FE polarized states. The doping concentrations on VSeF layer are $1.6 \times 10^{13}\,cm^{-2}$, $0\,cm^{-2}$, $3.1 \times 10^{13}\,cm^{-2}$ and $-1.5 \times 10^{13}\,cm^{-2}$ in $VSeF/Al_2Se_3$ (↑), $VSeF/Al_2Se_3$ (↓), $VSeF/biAl_2Se_3$ (↑) and $VSeF/biAl_2Se_3$ (↓) heterostructures, respectively. Here, the positive values represent electron doping and negative values represent hole doping. We found that the Curie temperature increases with the carrier doping concentration. And the hole carriers with smaller effective mass are more beneficial for the enhancement of T_c than electron carriers. Therefore, bilayer Al_2Se_3 FE gates not only can control the carriers' spin polarization in VSeF channel layer, but also can enhance the Curie temperature of VSeF.

Furthermore, we revealed that such nonvolatile electric control of spin polarization can be applied to other 2D BMS/FE multiferroic heterostructures, where the choices of FE gates and 2D BMS channel materials are abundant. For example, both bilayer Ga_2Se_3 and In_2Se_3 FE substrates show reversible interfacial doping effect which results in the manipulation of carriers' type and spin-polarized direction in VSeF layer by switching the ferroelectric polarized state (Supplementary Fig. 18 and Supplementary Fig. 19). However, since the band alignment between VSeF and different FE substrates is different, the interfacial charge transfer in VSeF/FE heterostructures would be different, which is related to the FE material species and FE polarized states. By calculating the charge density difference in different VSeF/FE heterostructures (Supplementary Fig. 17), we summarized the doping concentration of different FE gates in Fig. 5c. The carrier doping concentrations from different FE gates are all on the order of $10^{13}\,cm^{-2}$, which is comparable with the traditional gate-voltage applied[51]. Besides, we verified the nonvolatile control strategy is also achieved in $LaBr_2/triAl_2Te_3$ (trilayer Al_2Te_3) multiferroic heterostructure (Supplementary Fig. 20), where $LaBr_2$ has been predicted to be a 2D BMS[52]. For the other screened BMS VSF, the reversible control of carriers' spin polarization is also achieved in the $VSF/biGa_2S_3$ multiferroic heterostructure (Supplementary Fig. 21). These results indicate the feasibility and generality of our proposed nonvolatile electrical control strategy to BMS materials.

Devices based on $VSeF/Al_2Se_3$ and $VSeF/biAl_2Se_3$ heterostructures

Nanoscale devices are the inevitable trend of future technology development. Here, we suggested that the $VSeF/Al_2Se_3$ bilayer and $VSeF/biAl_2Se_3$ trilayer vdW heterostructures are promising structures for designing nanoscale spintronic devices. As shown in Fig. 6a, b, an atom-thick multiferroic memory device can be constructed based on the $VSeF/Al_2Se_3$ bilayer heterostructure. Since the electronic properties of the upper VSeF layer, either ferromagnetic half-metallic (100% spin-up polarization) or semiconducting, are controllable by the polarized state of Al_2Se_3, it serves as a channel material to be selectively conductive. Spin-up electrons can propagate through the VSeF ("on" state) for $VSeF/Al_2Se_3$ (↑) (Fig. 6a), while the electron transmission is blocked ("off" state) for $VSeF/Al_2Se_3$ (↓) (Fig. 6b). Here, data writing in the memory is realized by switching the ferroelectric polarized states, and data reading is realized by detecting the electrical signals.

As for $VSeF/biAl_2Se_3$ trilayer heterostructure, we designed a spin filter device (Fig. 6c, d). The spin polarization of the upper VSeF layer, either spin-up or spin-down, are controlled by the ferroelectric polarized state of bilayer Al_2Se_3. For $VSeF/biAl_2Se_3$ (↑), n-doped VSeF layer only allows spin-up electron carrier pass (Fig. 6c). When the polarization direction of bilayer Al_2Se_3 is reversed by an external electric field, the upper VSeF layer is p-type doped, only allowing spin-down hole carrier pass (Fig. 6d). Therefore, the manipulation of spin-polarized current can be achieved in this device.

DISCUSSION

In summary, based on first-principles calculations, we reported an intrinsic 2D BMS VSeF and unveiled the microscopic origin of its BMS feature. The non-negligible interorbital Coulomb repulsion between occupied states and unoccupied states in V^{3+} ([Ar]$3d^2$) and spin exchange splitting are both responsible for its bipolar character. Furthermore, we proposed a nonvolatile way to manipulate the spin polarization of BMS by introducing the ferroelectric gate. As embodied in the 2D BMS VSeF, the magnetic half-metal/semiconductor switching and spin-up/spin-down polarization switching in VSeF can be realized by manipulating the electric polarization of monolayer FE Al_2Se_3 and bilayer FE Al_2Se_3 in $VSeF/Al_2Se_3$ bilayer and $VSeF/biAl_2Se_3$ trilayer multiferroic heterostructures, respectively. These reversible switching endow VSeF with many promising applications in nanodevices, such as atom-thick multiferroic memory and spin filter. We find that the interfacial doping effect from FE gates also plays a role to enhance the Curie temperature of VSeF layer, which facilitates the utilization of spintronic nanodevices based on VSeF BMS. Finally, it's worth noting that our proposed nonvolatile way to manipulate spin polarization in BMS materials by introducing FE gates was feasible and general, where the choices of BMS channel materials and FE gates are abundant. Therefore, our work not only reports an intrinsic 2D BMS, but also provides a feasible and general approach to achieve nonvolatile electrical control of 2D BMS.

METHODS

All first-principles calculations were performed by using the density functional theory (DFT), as implemented in the Vienna ab initio simulation package (VASP)[53]. The Perdew-Burke-Ernzerhof generalized gradient approximation (PBE-GGA)[54] was employed to deal with the electron exchange-correlation potentials. The projector-augmented-wave (PAW)[55] pseudopotentials were applied to describe the electron-ion interaction with a plane-wave cutoff of 520 eV. $3p^6 3d^4 4s^1$ of V, $4s^2 4p^4$ of Se, $3s^2 3p^4$ of S, $2s^2 2p^5$ of F, $3s^2 3p^1$ of Al, $4s^2 4p^1$ of Ga, $5s^2 5p^1$ of In, $5s^2 5p^6 5d^1 6s^2$ of La, $4s^2 4p^5$ of Br and $5s^2 5p^4$ of Te electronic configurations were treated as valence electrons, respectively. The strong Coulomb interaction between V-3*d* electrons is corrected by the DFT + U method in the Dudarev form[56], where the effective U parameter $U_{eff} = U - J$ was applied to the d orbitals of V atoms. The hybrid Heyd-Scuseria-Ernzerhof functional (HSE06)[57] was also used to obtain the band structure for VSeF monolayer. A 20 Å thickness vacuum layer was introduced along the *z*-axis in all calculations. Ab initio molecular dynamical simulations (AIMD) were performed under an NVT ensemble. The ferroelectric reversal barrier was calculated using climbing nudged elastic band (CI-NEB) method[58,59]. The interlayer van der Waals interaction was considered by using the DFT-D3 method of Grimme[60] for $VSeF/Al_2Se_3$, $VSeF/biAl_2Se_3$, $VSeF/biGa_2Se_3$,

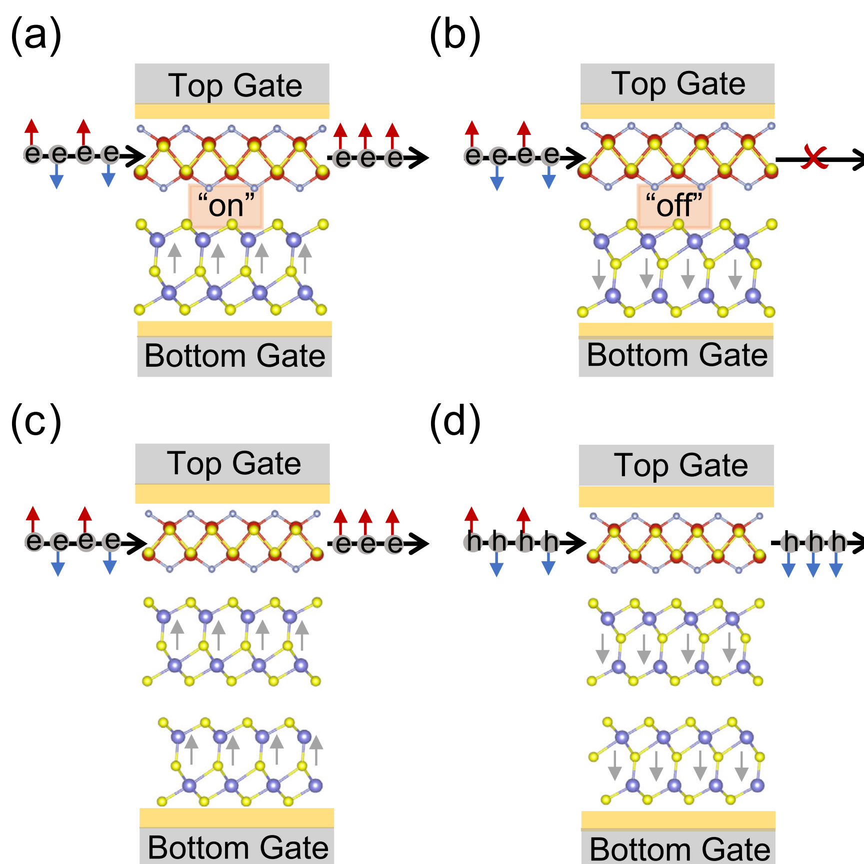

Fig. 6 Two types of spin FETs. a, b Atom-thick multiferroic memory based on the VSeF/Al_2Se_3 bilayer heterostructure, where the data writing and reading can be achieved by manipulating the ferroelectric polarization states of Al_2Se_3 monolayer and measuring the conductivity of VSeF channel, respectively. The red and blue arrows represent carriers' spin-up and spin-down polarized orientations, respectively. **c, d** spin filter based on the VSeF/biAl_2Se_3 trilayer heterostructure, where the carriers' spin-polarized orientation and carriers' type (electron/hole) in the VSeF channel depend on the ferroelectric polarization states of bilayer FE Al_2Se_3.

VSeF/biIn_2Se_3, $LaBr_2$/triAl_2Te_3 (trilayer Al_2Te_3) and VSF/biGa_2S_3 heterostructures. A dipole correction was applied to eliminate spurious dipole-dipole interaction between periodic images. Atomic positions and lattice parameters were fully relaxed until the force acting on each atom was less than 10^{-3} eV Å^{-1} for VSeF monolayer, VSF monolayer and $LaBr_2$ monolayer. For VSeF/Al_2Se_3, VSeF/biAl_2Se_3, VSeF/biGa_2Se_3, VSeF/biIn_2Se_3, $LaBr_2$/triAl_2Te_3 and VSF/biGa_2S_3 heterostructures, due to the lattice mismatch, we fixed the lattice constant of VSeF, VSF and $LaBr_2$ ferromagnetic layer and only relaxed the atomic positions with the force convergence criterion of 10^{-2} eV Å^{-1}. The phonon spectrum was calculated using the finite-displacement method implemented in the PHONOPY code[61]. The dynamical Monte Carlo (MC) simulation based on the Heisenberg model was performed to estimate the magnetic transition temperature.

DATA AVAILABILITY

The data supporting the findings of this paper are available from the corresponding authors upon reasonable request.

CODE AVAILABILITY

The central code used in this paper is VASP. Detailed information related to the license and user guide are available at https://www.vasp.at.

Received: 3 November 2022; Accepted: 16 March 2023;
Published online: 03 April 2023

REFERENCES

1. Han, W., Kawakami, R. K., Gmitra, M. & Fabian, J. Graphene spintronics. *Nat. Nanotechnol.* **9**, 794–807 (2014).
2. Soumyanarayanan, A., Reyren, N., Fert, A. & Panagopoulos, C. Emergent phenomena induced by spin-orbit coupling at surfaces and interfaces. *Nature* **539**, 509–517 (2016).
3. Zutic, I., Fabian, J. & Das Sarma, S. Spintronics: fundamentals and applications. *Rev. Mod. Phys.* **76**, 323–410 (2004).
4. Huang, B. et al. Layer-dependent ferromagnetism in a van der Waals crystal down to the monolayer limit. *Nature* **546**, 270–273 (2017).
5. Gong, C. et al. Discovery of intrinsic ferromagnetism in two-dimensional van der Waals crystals. *Nature* **546**, 265–269 (2017).
6. Deng, Y. et al. Gate-tunable room-temperature ferromagnetism in two-dimensional Fe_3GeTe_2. *Nature* **563**, 94–99 (2018).
7. Geim, A. K. & Grigorieva, I. V. Van der Waals heterostructures. *Nature* **499**, 419–425 (2013).
8. Huang, B. et al. Electrical control of 2D magnetism in bilayer CrI_3. *Nat. Nanotechnol.* **13**, 544–548 (2018).
9. Matsukura, F., Tokura, Y. & Ohno, H. Control of magnetism by electric fields. *Nat. Nanotechnol.* **10**, 209–220 (2015).
10. Eerenstein, W., Mathur, N. D. & Scott, J. F. Multiferroic and magnetoelectric materials. *Nature* **442**, 759–765 (2006).
11. Gajek, M. et al. Tunnel junctions with multiferroic barriers. *Nat. Mater.* **6**, 296–302 (2007).
12. Scott, J. F. Data storage. Multiferroic memories. *Nat. Mater.* **6**, 256–257 (2007).
13. Fiebig, M., Lottermoser, T., Meier, D. & Trassin, M. The evolution of multiferroics. *Nat. Rev. Mater.* **1**, 16046 (2016).
14. Khomskii, D. Classifying multiferroics: mechanisms and effects. *Physics* **2**, 20 (2009).
15. Wang, W. et al. Tunning magnetism and anisotropy by ferroelectric polarization in 2D van der Waals multiferroic heterostructures. *Mater. Today Phys.* **27**, 100803 (2022).

16. Xue, F., Wang, Z., Hou, Y., Gu, L. & Wu, R. Control of magnetic properties of $MnBi_2Te_4$ using a van der Waals ferroelectric III_2-VI_3 film and biaxial strain. *Phys. Rev. B* **101**, 184426 (2020).
17. Gong, C., Kim, E. M., Wang, Y., Lee, G. & Zhang, X. Multiferroicity in atomic van der Waals heterostructures. *Nat. Commun.* **10**, 2657 (2019).
18. Li, Z. & Zhou, B. Theoretical investigation of nonvolatile electrical control behavior by ferroelectric polarization switching in two-dimensional $MnCl_3/CuInP_2S_6$ van der Waals heterostructures. *J. Mater. Chem. C* **8**, 4534–4541 (2020).
19. Zhao, Y., Zhang, J. J., Yuan, S. & Chen, Z. Nonvolatile electrical control and heterointerface-induced half-metallicity of 2D ferromagnets. *Adv. Funct. Mater.* **29**, 1901420 (2019).
20. Garcia, V. et al. Ferroelectric control of spin polarization. *Science* **327**, 1106–1110 (2010).
21. Sun, W. et al. Controlling bimerons as skyrmion analogues by ferroelectric polarization in 2D van der Waals multiferroic heterostructures. *Nat. Commun.* **11**, 5930 (2020).
22. Cheng, H.-X., Zhou, J., Wang, C., Ji, W. & Zhang, Y.-N. Nonvolatile electric field control of magnetism in bilayer CrI_3 on monolayer In_2Se_3. *Phys. Rev. B* **104**, 064443 (2021).
23. Lu, Y. et al. Artificial multiferroics and enhanced magnetoelectric effect in van der Waals Heterostructures. *ACS Appl. Mater. Interfaces* **12**, 6243–6249 (2020).
24. Sun, W., Wang, W., Chen, D., Cheng, Z. & Wang, Y. Valence mediated tunable magnetism and electronic properties by ferroelectric polarization switching in 2D FeI_2/In_2Se_3 van der Waals heterostructures. *Nanoscale* **11**, 9931–9936 (2019).
25. Li, J., Li, X. & Yang, J. A review of bipolar magnetic semiconductors from theoretical aspects. *Fundam. Res.* **2**, 511–521 (2022).
26. Li, X., Wu, X., Li, Z., Yang, J. & Hou, J. G. Bipolar magnetic semiconductors: a new class of spintronics materials. *Nanoscale* **4**, 5680–5685 (2012).
27. Zhang, J., Zhao, B., Ma, C. & Yang, Z. Bipolar ferromagnetic semiconductors and doping-tuned room-temperature half-metallicity in monolayer MoX_3 (X=Cl, Br, I): An HSE06 study. *Phys. Rev. B* **103**, 075433 (2021).
28. Deng, J., Guo, J., Hosono, H., Ying, T. & Chen, X. Two-dimensional bipolar ferromagnetic semiconductors from layered antiferromagnets. *Phys. Rev. Mater.* **5**, 034005 (2021).
29. Luo, N., Si, C. & Duan, W. Structural and electronic phase transitions in ferromagnetic monolayer VS_2 induced by charge doping. *Phys. Rev. B* **95**, 205432 (2017).
30. Li, X. & Yang, J. Toward Room-Temperature Magnetic Semiconductors in Two-Dimensional Ferrimagnetic Organometallic Lattices. *J. Phys. Chem. Lett.* **10**, 2439–2444 (2019).
31. Sun, Z. et al. A new phase of the two-dimensional ReS_2 sheet with tunable magnetism. *J. Mater. Chem. C.* **6**, 1248–1254 (2018).
32. Sun, Y., Zhuo, Z. & Wu, X. Bipolar magnetism in a two-dimensional NbS_2 semiconductor with high Curie temperature. *J. Mater. Chem. C.* **6**, 11401–11406 (2018).
33. Li, X. & Yang, J. Bipolar magnetic materials for electrical manipulation of spin-polarization orientation. *Phys. Chem. Chem. Phys.* **15**, 15793–15801 (2013).
34. Lee, K. et al. Magnetic order and symmetry in the 2D semiconductor CrSBr. *Nano Lett.* **21**, 3511–3517 (2021).
35. Oganov, A. R. & Glass, C. W. Crystal structure prediction using ab initio evolutionary techniques: Principles and applications. *J. Chem. Phys.* **124**, 244704 (2006).
36. Wang, Y., Lv, J., Zhu, L. & Ma, Y. Crystal structure prediction via particle-swarm optimization. *Phys. Rev. B* **82**, 094116 (2010).
37. Gjerding, M. N. et al. Recent progress of the computational 2D materials database (C2DB). *2D Mater.* **8**, 044002 (2021).
38. Haastrup, S. et al. The Computational 2D Materials Database: high-throughput modeling and discovery of atomically thin crystals. *2D Mater.* **5**, 042002 (2018).
39. Wang, H., Qi, J. & Qian, X. Electrically tunable high Curie temperature two-dimensional ferromagnetism in van der Waals layered crystals. *Appl. Phys. Lett.* **117**, 083102 (2020).
40. Medici, L., Hassan, S. R., Capone, M. & Dai, X. Orbital-selective Mott transition out of band degeneracy lifting. *Phys. Rev. Lett.* **102**, 126401 (2009). de'.
41. Zhang, Y. Z., Foyevtsova, K., Jeschke, H. O., Schmidt, M. U. & Valenti, R. Can the Mott insulator TiOCl be metallized by doping? A first-principles study. *Phys. Rev. Lett.* **104**, 146402 (2010).
42. Zhuang, H. L. & Hennig, R. G. Stability and magnetism of strongly correlated single-layer VS2. *Phys. Rev. B* **93**, 054429 (2016).
43. Nguyen, T. P. T., Yamauchi, K., Oguchi, T., Amoroso, D. & Picozzi, S. Electric-field tuning of the magnetic properties of bilayer VI_3: a first-principles study. *Phys. Rev. B* **104**, 014414 (2021).
44. Glawion, S. et al. Electronic structure of the two-dimensional Heisenberg antiferromagnet VOCl: a multiorbital Mott insulator. *Phys. Rev. B* **80**, 155119 (2009).
45. Li, Y. et al. Rational design of heteroanionic two-dimensional materials with emerging topological, magnetic, and dielectric properties. *J. Phys. Chem. Lett.* **13**, 3594–3601 (2022).
46. Deng, J. et al. Screening and design of bipolar magnetic-semiconducting monolayers and heterostructures. *ACS Appl. Electron. Mater.* **4**, 3232–3239 (2022).
47. Ding, W. et al. Prediction of intrinsic two-dimensional ferroelectrics in In_2Se_3 and other III_2-VI_3 van der Waals materials. *Nat. Commun.* **8**, 14956 (2017).
48. Soleimani, M. & Pourfath, M. Ferroelectricity and phase transitions in In_2Se_3 van der Waals material. *Nanoscale* **12**, 22688–22697 (2020).
49. Wang, H. et al. Above room-temperature ferromagnetism in wafer-scale two-dimensional van der Waals Fe_3GeTe_2 tailored by a topological insulator. *ACS Nano* **14**, 10045–10053 (2020).
50. Zhu, W. et al. Interface-enhanced ferromagnetism with long-distance effect in van der Waals Semiconductor. *Adv. Funct. Mater.* **32**, 2108953 (2021).
51. Palacios, T. et al. High-performance E-mode AlGaN/GaN HEMTs. *IEEE Electron Device Lett.* **27**, 428–430 (2006).
52. Zhao, P. et al. Single-layer LaBr2: two-dimensional valleytronic semiconductor with spontaneous spin and valley polarizations. *Appl. Phys. Lett.* **115**, 261605 (2019).
53. Kresse, G. & Furthmuller, J. Efficiency of ab-initio total energy calculations for metals and semiconductors using a plane-wave basis set. *Comput. Mater. Sci.* **6**, 15–50 (1996).
54. Perdew, J. P., Burke, K. & Ernzerhof, M. Generalized gradient approximation made simple. *Phys. Rev. Lett.* **77**, 3865–3868 (1996).
55. Kresse, G. & Joubert, D. From ultrasoft pseudopotentials to the projector augmented-wave method. *Phys. Rev. B* **59**, 1758–1775 (1999).
56. Dudarev, S. L., Botton, G. A., Savrasov, S. Y., Humphreys, C. J. & Sutton, A. P. Electron-energy-loss spectra and the structural stability of nickel oxide: an LSDA +U study. *Phys. Rev. B* **57**, 1505–1509 (1998).
57. Heyd, J., Scuseria, G. E. & Ernzerhof, M. Hybrid functionals based on a screened Coulomb potential. *J. Chem. Phys.* **118**, 8207 (2003).
58. Zarkevich, N. A. & Johnson, D. D. Nudged-elastic band method with two climbing images: finding transition states in complex energy landscapes. *J. Chem. Phys.* **142**, 024106 (2015).
59. Henkelman, G., Uberuaga, B. P. & Jonsson, H. A climbing image nudged elastic band method for finding saddle points and minimum energy paths. *J. Chem. Phys.* **113**, 9901–9904 (2000).
60. Grimme, S. Semiempirical GGA-type density functional constructed with a long-range dispersion correction. *J. Comput. Chem.* **27**, 1787–1799 (2006).
61. Togo, A. & Tanaka, I. First principles phonon calculations in materials science. *Scr. Mater.* **108**, 1–5 (2015).

ACKNOWLEDGEMENTS

This work was supported by grants from the National Natural Science Foundation of China (61888102, 52102193, 52272172, 11974045), the Major Program of National Natural Science Foundation of China (92163206), the National Key Research and Development Program of China (2021YFA1201501), and the Strategic Priority Research Program of the Chinese Academy of Sciences (XDB30000000), and the Fundamental Research Funds for the Central Universities. Computational resources were provided by the National Supercomputing Center in Tianjin.

AUTHOR CONTRIBUTIONS

S.D. and J.P. conceived and supervised the research project. Y.L. performed the first-principles calculations and data analysis. Y.L. wrote the initial manuscript. All authors participated in discussing and editing the manuscripts.

COMPETING INTERESTS

The authors declare no competing interests.

ADDITIONAL INFORMATION

Supplementary information The online version contains supplementary material available at https://doi.org/10.1038/s41524-023-01005-8.

Correspondence and requests for materials should be addressed to Jinbo Pan or Shixuan Du.

Reprints and permission information is available at http://www.nature.com/reprints

Publisher's note Springer Nature remains neutral with regard to jurisdictional claims in published maps and institutional affiliations.

Open Access This article is licensed under a Creative Commons Attribution 4.0 International License, which permits use, sharing, adaptation, distribution and reproduction in any medium or format, as long as you give appropriate credit to the original author(s) and the source, provide a link to the Creative Commons license, and indicate if changes were made. The images or other third party material in this article are included in the article's Creative Commons license, unless indicated otherwise in a credit line to the material. If material is not included in the article's Creative Commons license and your intended use is not permitted by statutory regulation or exceeds the permitted use, you will need to obtain permission directly from the copyright holder. To view a copy of this license, visit http://creativecommons.org/licenses/by/4.0/.

© The Author(s) 2023